Applied Catalysis B: Environmental 300 (2022) 120736

Contents lists available at ScienceDirect

Applied Catalysis B: Environmental

journal homepage: www.elsevier.com/locate/apcatb

Band alignment of homojunction by anchoring CN quantum dots on g-C_3N_4 (0D/2D) enhance photocatalytic hydrogen peroxide evolution

Peijie Ma [a], Xu Zhang [a], Cong Wang [a,*], Zhiwei Wang [b], Kaiwen Wang [a], Yibo Feng [a], Jiaxing Wang [a], Yadi Zhai [a], Jiguang Deng [b,*], Lihua Wang [a], Kun Zheng [a,*]

[a] Beijing Key Lab of Microstructure and Properties of Solids, Faculty of Materials and Manufacturing, Beijing University of Technology, Beijing 100124, China
[b] Key Laboratory of Beijing on Regional Air Pollution Control, Beijing Key Laboratory for Green Catalysis and Separation, College of Environmental and Energy Engineering, Beijing University of Technology, Beijing 100124, China

ARTICLE INFO

Keywords:
H_2O_2
Carbon nitride
Quantum dots
Band alignment
Homojunction

ABSTRACT

Polymeric carbon nitride (C_3N_4) is a very attractive candidate to produce photocatalytic hydrogen peroxide (H_2O_2) due to its low-cost, metal-free characteristics. However, the low efficiency would limit its development to higher yields because of insufficient light absorption and electron-hole separation. Here, we developed a simple method to anchor CN quantum dots (QDs) onto g-C_3N_4 nanosheets to form a homojunction structure (HJ-C_3N_4), which could improve photocatalytic performance largely without introducing metal elements. Its superior efficiency is a result of the band alignment by the homojunction structure providing excellent electron-hole separation and QDs providing suppressed recombination. Simultaneously, the light responsiveness of QDs endows a wide spectrum-responsive adsorption and enhances the adsorption intensity. The H_2O_2 yield of the HJ-C_3N_4 reached 115 μmol L^{-1} h^{-1} in pure water by visible light, which has an 8.6x higher production than g-C_3N_4 nanosheets. The material design of 0D/2D homojunction could be extended to other materials with specific band alignment.

1. Introduction

Hydrogen peroxide (H_2O_2), as a clean, valuable, and multifunctional chemical, is widely used in the fields of biology, medicine, energy, and chemistry [1,2]. Compared with traditional industrial approaches with high energy consumption [3], the photocatalytic production of H_2O_2 using solar energy is sustainable and environmentally friendly [4,5]. Among the various photocatalysts, graphitic carbon nitride (g-C_3N_4) has been widely developed due to its simple synthesis at low cost, high exposure of active sites on a two-dimensional structure, environmental benignity, and visible light response capability [6,7]. More importantly, the active sites of g-C_3N_4 are suitable for O_2 activation in a two-electron reaction oxygen reduction reaction (ORR) [8]. In spite of that, the shortcomings of pristine g-C_3N_4, such as low quantum yield, poor charge separation and weaker light absorption [9]. With respect to these shortcomings, many strategies have been developed to modify the structures of g-C_3N_4 to improve its performance via band alignment, resulting in enlarged wavelengths of spectrum absorption, manipulation pathways of electron-hole (e^--h^+) separation [10] and suppressed photocarrier recombination [11]. Among them, numerous studies on loading metal material [12,13], especially noble metal elements [14–16], were investigated to provide significantly improved reaction efficiency, but the high-cost of noble metals and Schottky barriers provide an obstacle for this improvement during the catalytic process [17–19]. Therefore, there is an urgent demand for environmentally friendly metal-free catalytic materials to achieve proper band alignment.

Band alignment has been extensively studied by heterojunctions among semiconductors and metals with suitable energy levels. Following this strategy, the separation of e^--h^+ can be significantly enhanced in various composite systems and the proper energy level can be adjusted to favorable redox potentials [20–22]. For example, high efficiency photocatalytic water splitting is achieved by carbon nanodots (C dots) 0D/2D (zero-dimensional/two-dimensional) g-C_3N_4 modification [23] and a heterostructure of phosphorene/g-C_3N_4 2D/2D [24]. Excellent H_2O_2 production is also realized by 2D g-C_3N_4 and 2D black phosphorus (BP) [25]. However, the mismatch of lattice and energy band caused by two kinds of materials still leads to hindered charge

* Corresponding authors.
E-mail addresses: smartswang@bjut.edu.cn (C. Wang), jgdeng@bjut.edu.cn (J. Deng), kunzheng@bjut.edu.cn (K. Zheng).

https://doi.org/10.1016/j.apcatb.2021.120736
Received 4 July 2021; Received in revised form 2 September 2021; Accepted 16 September 2021
Available online 21 September 2021

separation and transport, which may give rise to carrier scattering and trapping near the interface for heterojunctions [26]. Therefore, a g-C_3N_4 homojunction catalyst without a Schottky barrier has been recently developed [27]. Yu et al. delicately realized tunable control of the band and the built-in electric field, achieving effective separation and movement of e^--h^+ by only manipulating the g-C_3N_4 [28]. Guo et al. rationally combined the energy band adjustment of the two kinds of g-C_3N_4 to form a 2D catalytic material, which has advantages of large interface contact area, excellent charge transfer ability, and favorable energy band structure [29]. Ye et al. increased photocatalytic efficiency five times by forming a 2D g-C_3N_4 homogeneous structure, specifically promoting efficient charge transfer and separation to a large extent [30]. Hence, the homojunction is emerging due to the rational combination of the 2D semiconducting polymer's advantages of large interfacial contact area, excellent charge transfer ability, and well-modulated band structures [31]. Furthermore, considering that 0D material of carbon nitride quantum dots (CN QDs [32]) has advantages for the suppression of the recombination of photocarriers, CN QDs anchored on 2D g-C_3N_4 may favor charge separation to improve the photocatalytic activity [33,34]. In particular, the up-conversion effect of QDs is specifically used to improve the absorption of long wavelength light (especially in the near-infrared band), and it can potentially enhance wider light absorption and narrower energy bands for matching redox potential in ORR [35,36]. Anchoring CN QDs on 2D g-C_3N_4 homojunctions can incorporate the above-mentioned advantages of separation enhancement, recombination suppression, and broad wavelength absorption.

Herein, we integrated 0D/2D C_3N_4 homojunction (HJ-C_3N_4) with controllable band alignment, which is utilized to solve the aforementioned problem of absorption and carrier separation. The optimized band gap can be reduced, corresponding to densest portion of solar energy. The obtained photocatalytic H_2O_2 yield of HJ-C_3N_4 reached 115 μmol L^{-1} h^{-1} due to the enhanced separation of photocarrier and lengthened absorption, which is nearly an order of magnitude higher than bare g-C_3N_4. Thus, we report a simple method to fabricate a 0D/2D homojunction, which provides a novel strategy to control its band structure. Based on that, separation enhancement, recombination suppression, and broad wavelength absorption can be achieved simultaneously. Thus, the strategy of 0D/2D homojunction material with band alignment can be readily extended to various photocatalysts in numerous reactions.

2. Experimental section

2.1. Catalyst preparation

2.1.1. Chemicals

Urea (CH_4N_2O, 99.9%), sodium citrate ($Na_3C_6H_5O_7{\cdot}2H_2O$, 99%), melamine ($C_3H_6N_6$, 99%), cyanuric acid ($C_3H_3N_3O_3$, 99%), were purchased from Aladdin company.

2.1.2. Preparation of g-C_3N_4 and CN QDs

g-C_3N_4 nanosheets: First, 2 g melamine and 4 g cyanuric acid were milled and mixed well into a fine powder using an agate mortar. Then, the mixed powder was heated at 520 °C in an unsealed crucible for 4 h with a ramp rate of 20 °C min^{-1} in a muffle furnace. Yellow solids were obtained and milled into powder. Finally, these solids were washed with deionized water and ethanol, and dried under vacuum at 60 °C.

CN QDs: 1.01 g melamine and 0.81 g sodium citrate were prepared individually, then milled and mixed well into a fine powder using an agate mortar. The mixed powder was heated at 180 °C in an unsealed crucible for 2 h with a ramp rate of 3 °C min^{-1} in a muffle furnace. Yellow solids were obtained and milled into powder. Then, these solids were washed with deionized ethanol 3 or 4 times, and subsequently dialyzed against pure water for 24 h. Finally, the solution was freeze-dried and milled to produce the yellow powders.

2.1.3. Preparation of HJ-C_3N_4

One gram of g-C_3N_4, 1.01 g melamine, and 0.81 g sodium citrate were prepared individually, then milled and mixed well into a fine powder using an agate mortar. The mixed powder was heated at 180 °C in an unsealed crucible for 2 h with a ramp rate of 3 °C min^{-1} in a muffle furnace. Yellow solids were obtained and milled into powder. Finally, these solids were washed with deionized water and ethanol 3 or 4 times, and dried under vacuum at 60 °C.

2.2. Photocatalytic evaluation

The photocatalytic activities were evaluated by the activation of oxygen under light irradiation ($\lambda \geq 400$ nm). A 300 W xenon lamp (Beijing Perfect Light, PLS-SXE300C) was chosen as a light source. During each photocatalytic performance, 0.02 g of catalyst was dispersed into 20 mL of pure water in a container (1 g L^{-1} catalyst), and the light intensity was about 109 mW cm^{-2}. After that, the dispersion was stirred a dark environment for 60 min to ensure the adsorption - desorption equilibrium among the catalyst, dissolved oxygen, and water before light irradiation. During the irradiation, 2 mL of the suspension was taken from the reaction cell at given time intervals, and then filtered to remove the catalysts. The concentrations of H_2O_2 generated were determined by determined using iodometric assays by UV–vis [37]. (Fig S6).

2.3. Characterization

X-ray diffraction patterns (XRD) of the samples were characterized at room temperature with a Bruker, D8 ADVANCE with Cu K_α radiation (λ = 0.15418 nm). Fourier Transform Infrared (FTIR) spectroscopy was performed with a Bruker Tensor-II using a standard KBr pellet technique, and X-ray photoelectron spectroscopy (XPS) analysis was obtained by a Thermo Fisher, ESCALAB 250Xi spectrometer with Al K_α ($h\nu$ = 1486.6 eV). Transmission electron microscope (TEM) images were examined with a FEI Titan Themis G2 microscope operated at 300 kV and FEI Titan E-TEM microscope operated at 300 kV. The photocatalytic production of H_2O_2 used iodometric assays measured by UV–vis methods; and the UV–vis absorption spectra of the samples were carried out on a HITACHI U-3900H spectrophotometer in the wavelength range of 300–700 nm ($BaSO_4$ as a reference material). Photoluminescence (PL) and time-resolved photoluminescence (TRPL) spectra were recorded on a HITACHI F-7000 and FLS-1000, respectively. Electrochemical measurement instruments and conditions are described in the Supporting Information.

3. Results and discussion

3.1. Characterization of HJ-C_3N_4, g-C_3N_4 and CN QDs

A schematic of the structural model of the homojunction catalyst is demonstrated in Fig. 1a. The homogeneous junction has 2D g-C_3N_4 nanosheets as the substrate and 0D QDs on the 2D surface (HJ-C_3N_4). A schematic diagram of the atomic structure is also shown as the functional groups around the CN QDs are mentioned, which is consistent with previous literature [32,38]. The morphologies of as-synthesized nanosheets and HJ-C_3N_4 powder are provided in Fig. S1. Their XRD patterns are shown in Fig. 1b, where the purple and blue curves show the patterns of HJ-C_3N_4 and g-C_3N_4 nanosheets, respectively. From them, a graphitic structure with an interplanar stacking distance of 0.325 nm aromatic units corresponding to a sharp diffraction peak (002) at 27.9° is observed. In addition, a diffraction peak (100) at 13.8° represents the in-planar repeating units and relates to the interplanar structural packing with an interlayer spacing of 0.675 nm [39], such as the hole-to-hole distance of the nitride pores in the crystal. Moreover, the peak of the homojunction structure shifts significantly, indicating that the interlayer spacing increases. It might be related to the doping of QDs on 2D

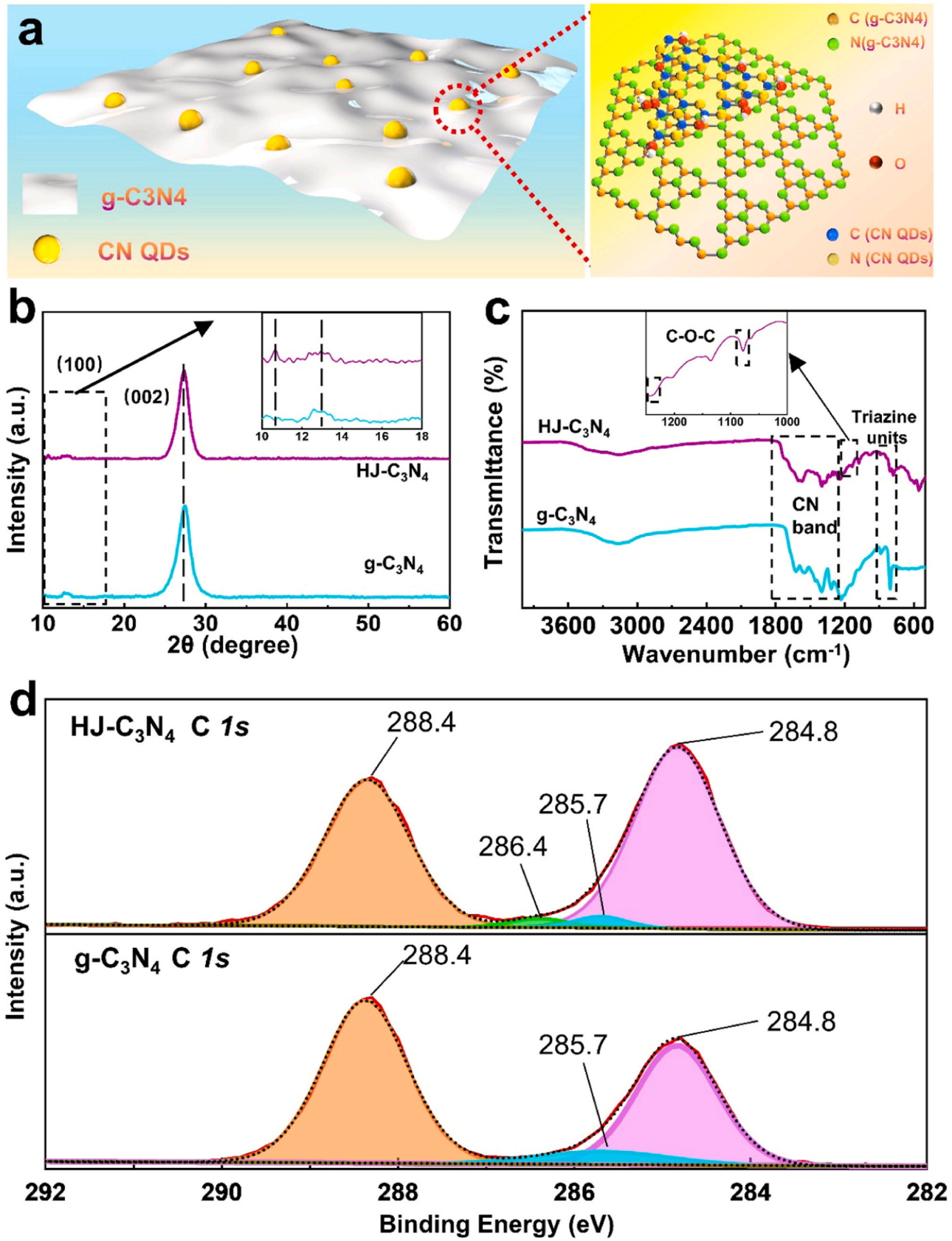

Fig. 1. (a) Diagram of the HJ-C_3N_4 catalyst model; (b) XRD patterns of bare g-C_3N_4 and HJ-C_3N_4; (c) FTIR spectra of bare g-C_3N_4 and HJ-C_3N_4; (d) C *1s* peak of bare g-C_3N_4 and HJ-C_3N_4.

materials, resulting in the fracture of the C and N bond or the addition of oxygen from CN QDs [34,40].

The structural composition of HJ-C_3N_4 are analyzed via FTIR spectroscopy (Fig. 1c). The absorption of peak at 812 cm^{-1} corresponds to the out-of-plane bending mode of the triazine units, which confirms the formation of the graphitic carbon nitride structure [41]. The peaks at 1238 $cm^{-1}$and 1070 cm^{-1} correspond to the stretching vibrations of the connected units of C-O-C group [12,42]. The peaks at 1315.7 cm^{-1} and 1241.2 cm^{-1} are assigned to the stretching vibration absorption of C-N═C (full condensation) and C–N–C (partial condensation), respectively. The peaks at 1645.4, 1564.5 cm^{-1}, and 1408.3 cm^{-1} all represent the stretching vibration modes of the repeating unit. Interestingly, compared with bare g-C_3N_4, HJ-C_3N_4 shows a decrease in specific peaks of the N—C═N bonds, indicating that the broken bonding of the initial 2D g-C_3N_4 might occur in the condition of the CN QDs doping [43]. Furthermore, XPS is used to further probe the chemical states of the HJ-C_3N_4 (Fig. 1d). First, the C *1 s* spectrum shows three deconvoluted peaks at 288.4 eV, 285.7 eV, 286.4 eV, and 284.8 eV. The major C peak at 288.4 eV is identified as sp^2-bonded carbon (N–C═N), and the weaker peak at 284.8 eV corresponds to graphitic carbon (C-C), which is usually observed in the XPS spectrum of carbon nitrides. The peak at 285.7 eV corresponds to C═C—N bonds, and the peak at 286.4 eV corresponds to the C—O bonds [44]. With the addition of QDs, the ratio of C—C bond/C—N bond in HJ-C_3N_4 decreases, which is accompanied by the opening of the C—C bond and the formation of a C—O bond, which can be proven by the oxygen content increases shown in the XPS survey (Fig. S4).

TEM is performed to further characterize the morphology and structure of HJ-C_3N_4. Fig. 2a is a low magnified TEM image showing the morphology of HJ-C_3N_4, in which the sheet structure was dispersed on carbon film of TEM grids. Fig. 2b is an enlarged image taken from the red framed region of Fig. 2a showing good dispersion of CN QDs on the g-C_3N_4 nanosheets. The CN QDs are uniformly distributed with a size distribution of QDs under high resolution, whose number of over 100 QDs (2–7 nm in diameter) is counted to obtain the averaged size of 4.3 nm in 2D g-C_3N_4 as shown in the inset. High resolution (HR)-TEM was carried out to identify the crystalline structure for individual CN QDs. Fig. 2c provides a HRTEM image showing high-quality single crystalline characteristics. In the image, the lattice spacing of d = 0.24 nm assigned to (100) planes of graphite correspond to the in-plane D-space lattice fringes of 0.237 nm of g-C_3N_4 [28]. Fig. 2d is a high-angle annular dark-field (HAADF) image of bare g-C_3N_4 with plenty of porous and plicate structures. Fig. 2e and f illustrate CN QDs with high crystalline structures anchored in the 2D g-C_3N_4 matrix as shown in the HAADF images, which are consistent with those obtained by TEM.

3.2. Reaction analysis of the catalyst

Notably, the band alignment in the homojunction has a unique effect on performance. To reveal the band structure of HJ-CN, the optical absorbance properties and valence band data (Fig. 3a and b) are obtained using UV–vis and Mott-Schottky results, respectively. As shown in Fig. 3a, the three catalysts clearly display an absorption in visible light regions. Interestingly, HJ-CN display a wider range of absorption than that of bare g-C_3N_4 due to the CN QDs combination. The bandgaps (Fig. 3b) of CN QDs, bare g-C_3N_4 and HJ-C_3N_4 are 2.20 eV, 2.86 eV, and 2.80 eV, respectively. Combined with the conduction band minimum (CBM) by Mott-Schottky results (Fig. S7), (CBM of CN QDs, bare g-C_3N_4, and HJ-C_3N_4 are − 0.74 eV, − 0.96 eV, and 0.92 eV) the complete energy band diagram is shown to have a type-I structure. And the valance band maximum (VBM) of CN QDs, bare g-C_3N_4, and HJ-C_3N_4 are

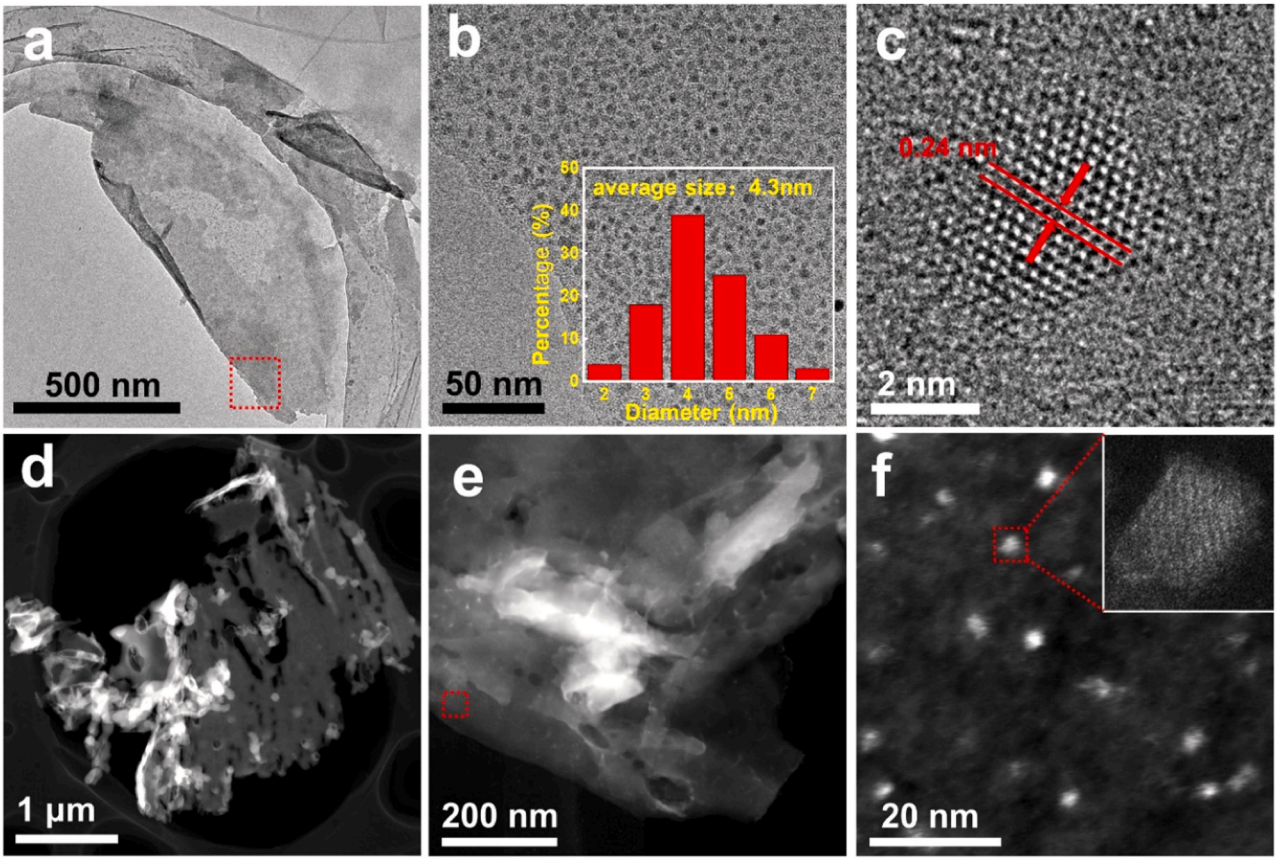

Fig. 2. (a) TEM image of HJ-C_3N_4; (b) Magnified TEM image of HJ-C_3N_4 of region of (a) marked in red and a size distribution of CN QDs; (c) HRTEM image of CN QDs anchored in 2D g-C_3N_4; (d) HAADF image of bare g-C_3N_4; (e) and (f) HAADF images of HJ-C_3N_4.

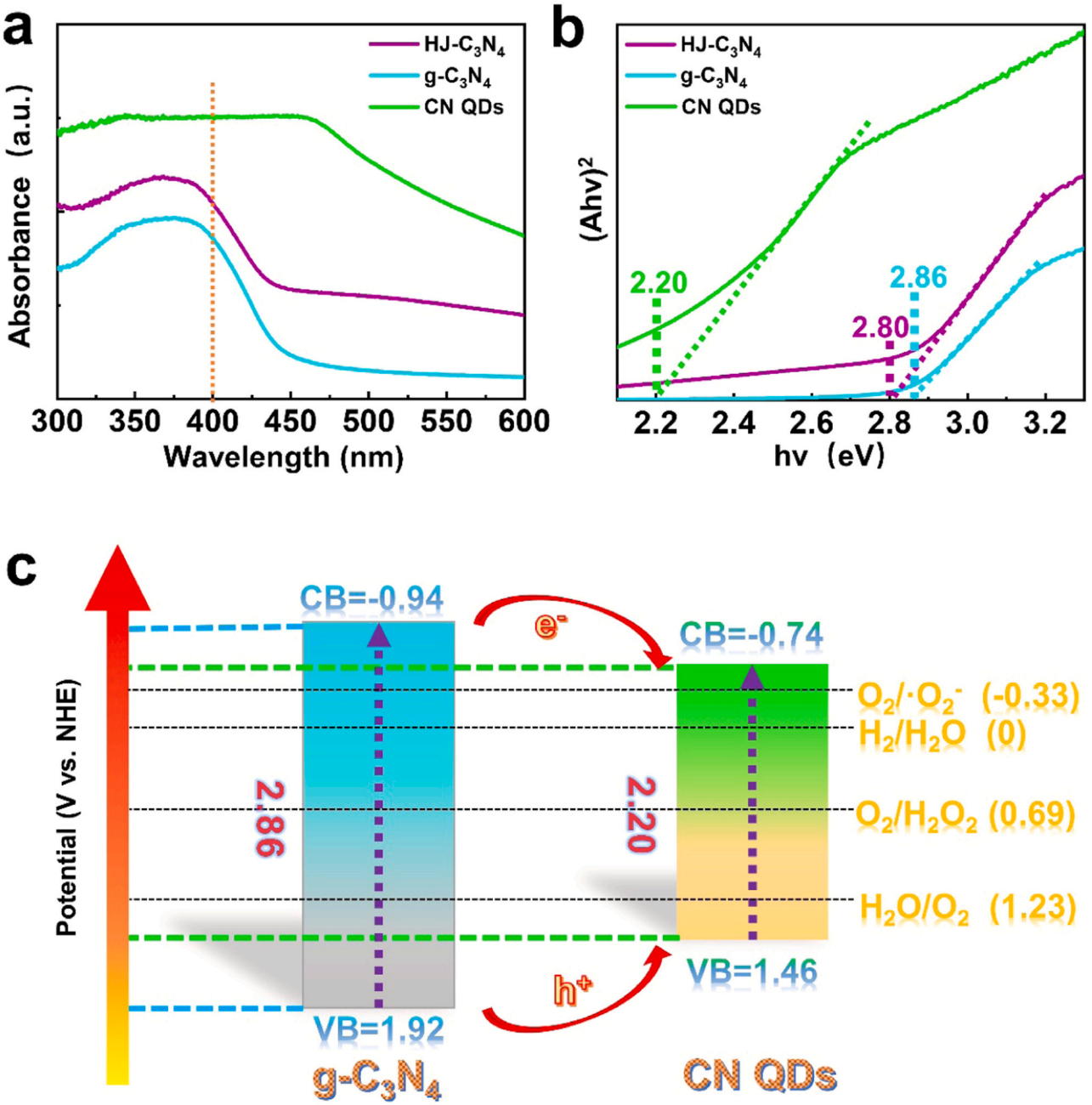

Fig. 3. (a) UV–vis absorption spectra and (b) $(ah\nu)^2$ versus hν curve of CN QDs, bare g-C_3N_4, and HJ-C_3N_4; (c) The estimated band structure of CN QDs and bare g-C_3N_4.

1.46 eV, 1.92 eV, and 1.88 eV, which is also verified by valence band values in VB-XPS 1.44 eV, 1.94 eV, and 1.84 eV, respectively (Fig. S12). That is to say, the VBM is consistent with the result calculated by band gap and CBM. The band structures of the catalysts are given as Fig. 3c. The values of CB, VB and the bandgap of HJ-C_3N_4 are located between the CN QDs and bare g-C_3N_4. A type-I homojunction band structure is usually considered as an easier recombination. In contrast, the type-I structure in this work ascribed to CN QDs has an advantage of electron-trapping with increased photocarrier lifetimes. Moreover, the smaller bandgap due to its size effect and quantum limiting effect provides a benefit of visible light absorption [35]. Therefore, developing band alignment of type-I photocatalysts is a novel strategy for photocatalytic site development. Furthermore, the homojunction ensures the photocarrier can move from the 2D g-C_3N_4 to the 0D CN QDs in the same substrate in a non-stoichiometric fashion [45].

UV–vis provides evidence for the expression of light absorption capacity. Hence, CN QDs enhance the light absorption intensity in visible wavelength and the increase of light absorption in wide-wavelength especially the type-I structure accompanied by narrow band gaps. And further analysis of carrier behavior is needed.

3.3. *Structure-catalytic performance relationship of bare g-C_3N_4 and HJ-C_3N_4*

To reveal the mechanism of the homojunction with enhanced performance, the photoelectron effect is clarified by electronic measurement and spectroscopy. The transient photocurrent response (TPR) was measured under O_2 to reflect that HJ-C_3N_4 has enhanced separation ability of photogenerated carriers (Fig. 4a). It shows that not only the heterojunction, but the homojunction also has a great advantage in

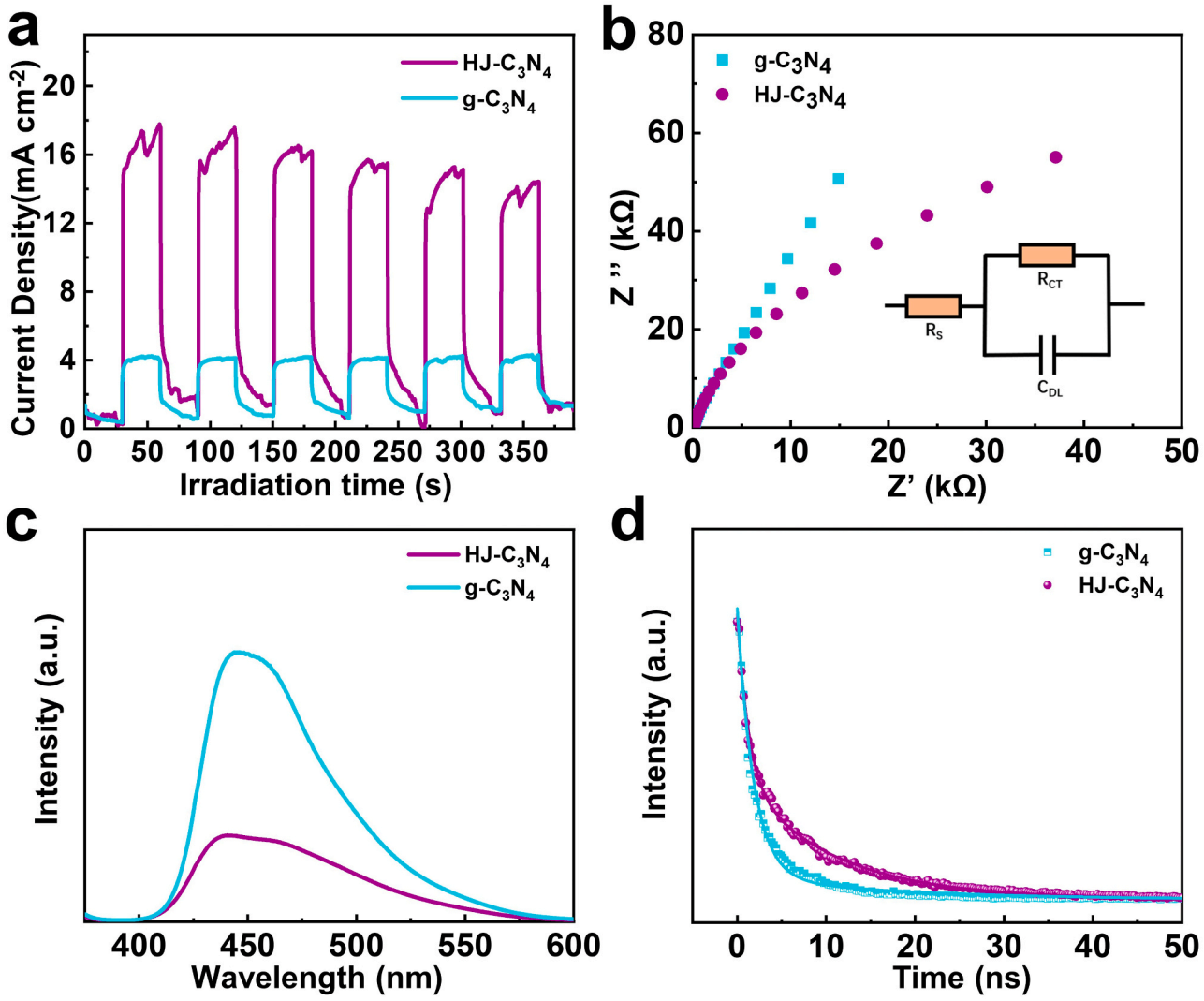

Fig. 4. (a) TPR curves and (b) EIS Nyquist plots of bare g-C_3N_4 and HJ-C_3N_4; (c) PL spectra and (d) TRPL spectra of bare g-C_3N_4 and HJ-C_3N_4.

ensuring the efficiency of e^--h^+ separation. Moreover, electrochemical impedance spectroscopy (EIS), as shown in Fig. 4b, is used to confirm the efficient separation of photogenerated electrons, thereby showing the electrical conductivity is dominated by the CN QDs anchored on 2D g-C_3N_4. The Nyquist plot consists of one dominant semicircle, which is related to the charge transfer resistance at the sample/electrolyte interface [46]. The diameter of the semicircle on the EIS plot of HJ-C_3N_4 is less than that of bare g-C_3N_4, suggesting the separation and transfer efficiency of photogenerated e^--h^+ pairs are greatly increased by homojunction formation. To avoid the inhibition of carrier transfer caused by incompatibility of the two materials in heterojunction, the homojunction gives full play to the excellent transport e^--h^+ of g-C_3N_4. The charge transfer advantage of the homojunction is benefit from the compatibility of the same material [26].

To investigate the recombination processes of photogenerated e^--h^+ pairs in photocatalysts, PL spectra measurements were also conducted (Fig. 4c). An excitation wavelength at 320 nm of PL spectra shows that the intensity of HJ-C_3N_4 is much smaller, indicating that the recombination of photocarriers on HJ-C_3N_4 was significantly suppressed. According to the energy band structure (Fig. 3c), e^- and h^+ move to QD, and the type-I structure is generally considered to be favorable for carrier recombination, however, the inhibition of carrier recombination shows that the addition of CN QDs could avoid it. By seriously analyzing and researching, the level of defects brought from the oxygen-containing groups is the main reason [34,47]. To analyze the kinetic behavior, TRPL spectroscopy is utilized to evaluate the charge separation dynamics processes (Fig. 4d). The lifetime of HJ-C_3N_4 (4.92 ns) is longer than that of bare g-C_3N_4 (3.28 ns) (Table. S1). Combined with the results of PL and TRPL, it can be concluded that HJ-C_3N_4 has a larger number of photoelectrons and longer lifetime of photoinduced e^--h^+ pairs, which has a strong influence on the photocatalytic H_2O_2 production on HJ-CN. Although the pure CN QDs have a lower intensity of PL (Fig. S9a), the durability of pure CN QDs is poor with a decrease of H_2O_2 production in a short period (Fig. S9d and Fig. S10). The instability of the surface group is the cause, which is consistent with previous work [48].

Therefore, the introduction of CN QDs on the surface of the 2D g-C_3N_4 not only leads to the efficient separation of e^--h^+ pairs, long carrier life and excellent charge transfer, but it also can increase the stability of CN QDs.

3.4. *Catalytic performance of bare g-C_3N_4 and HJ-C_3N_4*

As a result of 0D/2D type-I band homojunction structure, a higher photocatalytic performance was obtained. Fig. 5 provides a photocatalytic hydrogen peroxide production of various catalysts conducted and monitored under O_2-equilibration of pure water (absence of organic electron donors) in light irradiation ($\lambda \geq 400$ nm) at room temperature. As shown in Fig. 5a, H_2O_2 can rapidly generate over HJ-C_3N_4 and the

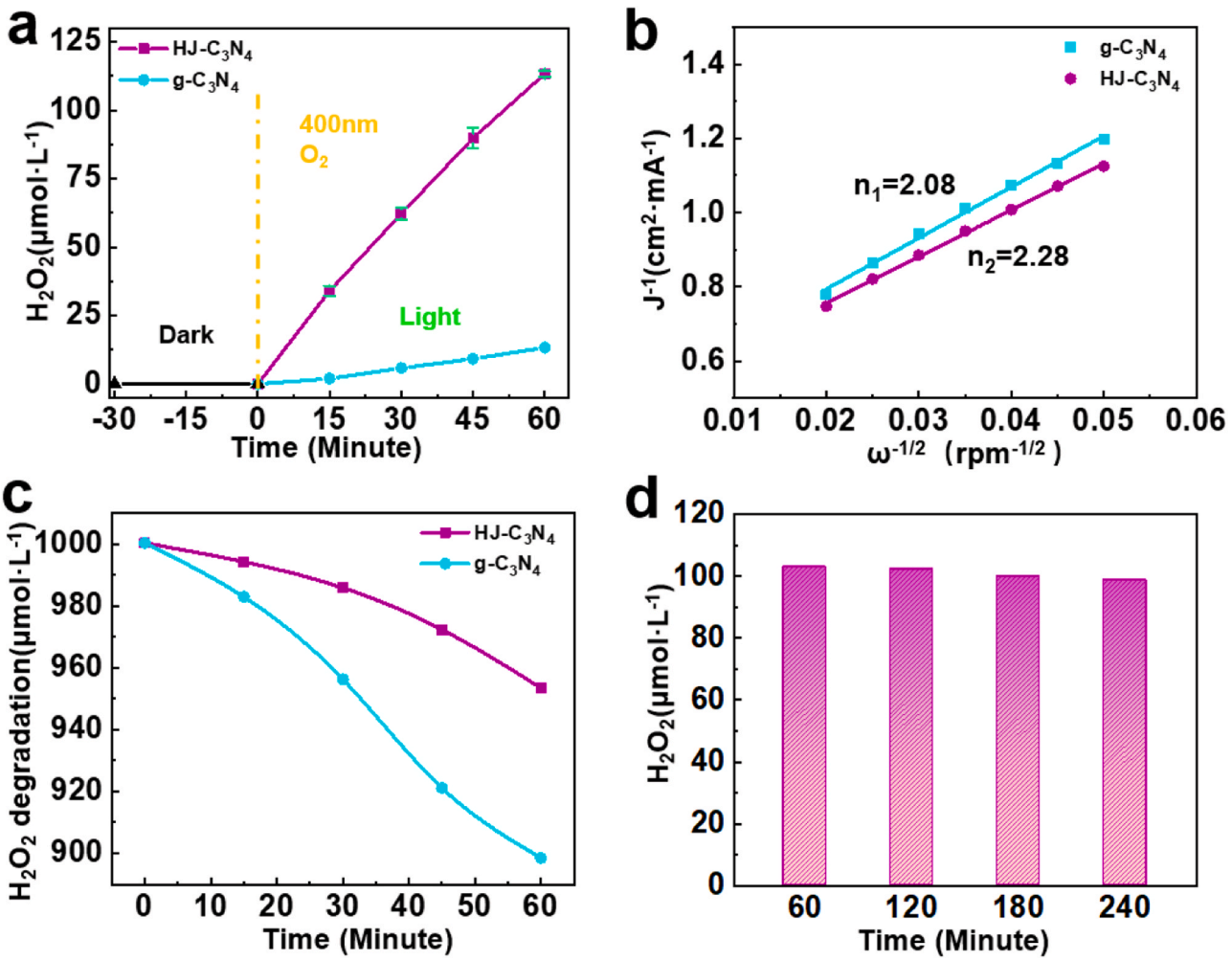

Fig. 5. (a) Light-driven H_2O_2 formation over different catalysts in 60 min. Reaction conditions: H_2O (20 mL), catalyst (20 mg, 1 g L^{-1}), O_2-equilibrated, 400 nm, 25 °C; (b) Koutecky-Levich plots of the ORR data measured by RDE analysis for bare g-C_3N_4 and HJ-C_3N_4; (c) Photocatalytic degradation of H_2O_2 on bare g-C_3N_4 and HJ-C_3N_4 under visible light irradiation: H_2O (20 mL), catalyst (20 mg, 1 g L^{-1}); (d) Stability testing of HJ-C_3N_4.

amounts of formed H_2O_2 can reach 115 μmol over 1 h, which is about 8.6 times that of bare g-C_3N_4 (14 μmol over 1 h) and is comparable to noble metal Pt on C_3N_4 [16]. To investigate O_2 reduction, which is under a two-electron reaction to H_2O_2, electrochemical rotating disk electrode (RDE) analysis of the oxygen reduction reaction was utilized. The details on RDE measurements are provided in SI (Fig. S8). The linear sweep voltammetry (LSV) curve data were analyzed using Koutecky-Levich (K–L) plots, and the data with the slope of linear fitting to obtain the average number of electrons (n) involved in the overall O_2 reduction was calculated (Fig. 5b). The n values for bare g-C_3N_4 and HJ-C_3N_4 are 2.08 and 2.28, suggesting that both of them are typical two-electron reactions, and the catalyst is highly selective for hydrogen peroxide production [49]. Meanwhile the decomposition of H_2O_2 under the same conditions is effectively inhibited (Fig. 5c) by HJ-C_3N_4. The related mechanism of a better performance for production and lower efficiency for decomposition contains the following: the thermodynamic instability analysis for the rate of formation decomposition and the impact of structure on performance behavior. The result was shown in Fig. S14 after calculation, the generation of H_2O_2 was regarded as the zero-order production constant k_f (the rate of H_2O_2 formation), and the decomposition process was the first-order rate constant k_d (the rate of H_2O_2 decomposition) [50,51]. k_f value of g-C_3N_4 and HJ-C_3N_4 are 2.8436 μmol min^{-1} and 0.163 μmol min^{-1}, and k_d value of g-C_3N_4 and HJ-C_3N_4 are 0.00996 min^{-1} and 0.02378 min^{-1}, respectively. With the addition of CN QDs in homojunction samples, the decomposition rate decreases while the productive rate increases significantly, thus the Fig. 5c shows decomposition decrease of homojunction is not only due to the suppression in the decomposition diagram, but also the generation of H_2O_2 is enhanced by the 0D/2D catalytic sites at the same time.

Moreover, the yield of H_2O_2 does not significantly decrease after four cycle experiments within the 4 h photocatalytic period, suggesting high stability of the homogeneous synthesized junction material (Fig. 5d). The HJ-C_3N_4 catalysts with homogeneous structure increase yield without selectivity losses, maintain stability, and reduce decomposition rates. We summarize recent progress in the pure water system (Table 1.). In the table, the H_2O_2 yield of this work is the highest among metal-free catalysts and comparable with the yield of the catalysts containing precious metals. It fully reflects that the HJ-C_3N_4 obtained by simple and environmental protection method has a great application prospect.

Compared with the widely-investigated type-II band structures in various photocatalysts, the design of the type-I band structure via band alignment is not broadly studied [20], which is usually considered to have recombined, photoinduced carriers [22]. The prerequisite of this strategy is the excellent suppression of carrier's recombination, which can be achieved by QDs with many defective energy levels. The reason is that the existence of coordinated oxygen with terminal functional groups can induce the defective energy level [12]. Besides, XPS results verified that oxygen appears and surrounds the CN QDs (Fig. S4), which was further confirmed by TEM-EDX (Energy Dispersive X-Ray Spectroscopy) (Fig. S3). The fracture might lead to an increase of lattice

Table 1
Comparison of photocatalytic H_2O_2 production.

Photocatalysts	Dosage ($g\ L^{-1}$)	Reaction solution	Light source	H_2O_2 production activity ($\mu mol\ g^{-1}$)	Refs.
HJ- C_3N_4	1.00	Water (20 mL)	300 W XL ($\lambda > 320$ nm)	115 (1 h)	This work
g-C_3N_4/PDI	1.67	Water (30 mL)	2 kW XL ($\lambda > 420$ nm)	21.08 (1 h)	[52]
g-C_3N_4/PDI/rGO	1.67	Water (30 mL)	2 kW XL ($\lambda > 420$ nm)	24.17 (1 h)	[8]
3DOM g-C_3N_4-PW_{11}	1.00	Water (100 mL)	300 W XL ($\lambda > 320$ nm)	35 (1 h)	[50]
Ag@U-g-C_3N_4-NS	1.00	Water (100 mL)	300 W XL ($\lambda > 420$ nm)	67.50 (1 h)	[15]
g-C_3N_4-CoWO	1.00	Water (100 mL)	300 W XL ($\lambda > 420$ nm)	9.7 (1 h)	[2]
OCN-500	1.00	Water (50 mL)	300 W XL ($\lambda > 420$ nm)	106 (1 h)	[12]
Cv-g-C_3N_4	1.00	Water (100 mL)	300 W XL ($\lambda > 320$ nm)	92 (1 h)	[5]
melam/WO_3	1.00	Water (10 mL)	435 nm LED	19 (6 h)	[37]
$PI_{5.0}$-NCN	1.00	Water (50 mL)	300 W XL ($\lambda > 420$ nm)	120 (2 h)	[53]
Co_1/AQ/C_3N_4	0.50	Water (12 mL)	300 W XL (AM 1.5 G)	62 (1 h)	[54]
Pd/APTMS/TiO_2	0.50	Water (10 mL)	300 W XL (AM 1.5 G)	150 (1 h) (Ph = 3)	[55]
Au/APTMS/TiO_2	0.50	Water (10 mL)	300 W XL (AM 1.5 G)	70 (1 h) (Ph = 3)	[55]
Pt@β-CD/C_3N_4-M	1	Water (60 mL)	300 W XL ($\lambda > 400$ nm)	147.1 (1 h)	[16]

spacing corresponding to an XRD peak shift. Moreover, FTIR confirms that the C-O-C bands obviously increase in HJ-C_3N_4 with intralayer and interlayer structures, which may allow for easier carrier transport. In previous work, the oxygen-terminal functional group contributes to the defect energy levels of CN QDs in the band gap of pristine g-C_3N_4, which may prevent recombination of photoinduced carriers, and even directly promote the production of H_2O_2 [34,35,56]. Consistently, CN QDs on 2D g-C_3N_4 have a better performance due to recombination prevention and the carrier life is improved.

Excellent electron-hole separation ability is summarized as follows: 1) The junction formed by the two portions in catalyst promotes electron-hole separation. 2) The defective energy level caused by oxygen-containing functional groups in CN QDs can inhibit electron-hole recombination.

More importantly, the CN QDs can provide the unique broad-spectrum response for the photocatalytic reaction (Fig S9b). Fig. S9c shows that HJ-C_3N_4 has a certain yield in the near-infrared band light ($\lambda > 600$ nm), and the incident light intensity is only one fourth that of visible light ($\lambda > 400$ nm). However, the bare CN QDs show poor stability in the photocatalytic production of H_2O_2 as shown in Fig. S9d and Fig. S10. Thus, by forming homojunction structures, the approach not only forms a bond to reduce the degradation of CN QDs, it also extends the absorption range.

The extending light absorption summarized as follows: 1) The CN QDs with narrow bandwidth in type-I homojunction have the advantages of unique light absorption enhancement, up-conversion effect and the utilization of near-infrared band light. 2) The 2D substrate has no obvious influence for capability of visible light absorption.

In this work, combined with the intrinsic advantages of large interfacial contact area, excellent charge transfer ability, and well-modulated band structures, type-I homojunction of 0D/2D provides a new way to improve efficiency. Although a few studies on the C_3N_4 homojunction and achievements of enhanced separation have been made, more materials should be further developed to rationally design better photocatalysts in the future.

4. Conclusions

Band alignment of homojunction materials is successfully prepared via anchoring of CN QDs on 2D C_3N_4 nanosheets. High efficiency of photocatalytic hydrogen peroxide production with 115 $\mu mol\ L^{-1}\ h^{-1}$ in pure water was achieved, which is more than 8.6 times that of bare g-C_3N_4. The enhanced efficiency is ascribed to the band alignment of the type-I homogeneous structure, which has excellent e^--h^+ separation ability and recombination suppression. HJ-C_3N_4 also made full use of wide-wavelength absorption in solar spectra via CN QDs anchoring, which greatly extends the absorption edge to nearly 600 nm. Moreover, the recombination of carriers on CN QDs can be applied in type-I homojunctions to avoid the efficiency decrease in other type-I structure materials. Thus, owing to band alignment, the active sites on the homojunction not only have more photoinduced carriers, but they also suppress recombination. Besides, the type-I homojunction further increases the stability of the CN QDs. Thus, a simple approach is developed to obtain 0D/2D homojunction g-C_3N_4, which can make use of the wide spectrum absorption of QDs and the homojunction structure for effective charge separation. Efficient photocatalytic H_2O_2 generation provides non-toxic and sustainable benefits, which can be applied to environmental and biological applications. Remarkably, this material design strategy of 0D/2D band alignment provides a new toolbox for highly efficient and selective photocatalysts.

CRediT authorship contribution statement

Peijie Ma prepared and characterized samples, tested the properties, Xu Zhang and Jiaxing Wang assisted with the prepared samples and tested the properties, Zhiwei Wang and Kaiwen Wang assisted with the characterized samples. Yadi Zhai and LihuaWang assisted and guided the aberration-corrected HRTEM and HAADF-STEM, Peijie Ma, Cong Wang, Jiguang Deng and Kun Zheng analyzed the experimental results and wrote the manuscript. Xu Zhang, Yibo Feng and Jiguang Deng made helpful comments on the manuscript. Kun Zheng led the entire project. All authors read the manuscript and contributed to the discussion of the results.

Declaration of Competing Interest

The authors declare that they have no known competing financial interests or personal relationships that could have appeared to influence the work reported in this paper.

Acknowledgment

This work is supported by the National Natural Science Foundation of China (11774016 and 21622701); Beijing Outstanding Young Scientists Projects (BJJWZYJH01201910005018); Natural Science Foundation of Beijing Municipality (Z180014).

Appendix A. Supporting information

Supplementary data associated with this article can be found in the online version at doi:10.1016/j.apcatb.2021.120736.

References

[1] Y. Yang, C. Zhang, D. Huang, G. Zeng, J. Huang, C. Lai, C. Zhou, W. Wang, H. Guo, W. Xue, R. Deng, M. Cheng, W. Xiong, Boron nitride quantum dots decorated ultrathin porous g-C_3N_4: intensified exciton dissociation and charge transfer for promoting visible-light-driven molecular oxygen activation, Appl. Catal. B: Environ. 245 (2019) 87–99.
[2] S. Zhao, X. Zhao, Insights into the role of singlet oxygen in the photocatalytic hydrogen peroxide production over polyoxometalates-derived metal oxides incorporated into graphitic carbon nitride framework, Appl. Catal. B: Environ. 250 (2019) 408–418.

[3] J.M. Campos-Martin, G. Blanco-Brieva, J.L. Fierro, Hydrogen peroxide synthesis: an outlook beyond the anthraquinone process, Angew. Chem. Int. Ed. Engl. 45 (2006) 6962–6984.

[4] H. Fattahimoghaddam, T. Mahvelati-Shamsabadi, B.-K. Lee, Enhancement in photocatalytic H_2O_2 production over g-C_3N_4 nanostructures: a collaborative approach of nitrogen deficiency and supramolecular precursors, ACS Sustain. Chem. Eng. 9 (2021) 4520–4530.

[5] S. Li, G. Dong, R. Hailili, L. Yang, Y. Li, F. Wang, Y. Zeng, C. Wang, Effective photocatalytic H_2O_2 production under visible light irradiation at g-C_3N_4 modulated by carbon vacancies, Appl. Catal. B: Environ. 190 (2016) 26–35.

[6] D. Deng, K.S. Novoselov, Q. Fu, N. Zheng, Z. Tian, X. Bao, Catalysis with two-dimensional materials and their heterostructures, Nat. Nanotechnol. 11 (2016) 218–230.

[7] X. Wang, K. Maeda, A. Thomas, K. Takanabe, G. Xin, J.M. Carlsson, K. Domen, M. Antonietti, A metal-free polymeric photocatalyst for hydrogen production from water under visible light, Nat. Mater. 8 (2009) 76–80.

[8] Y. Kofuji, Y. Isobe, Y. Shiraishi, H. Sakamoto, S. Tanaka, S. Ichikawa, T. Hirai, Carbon nitride-aromatic diimide-graphene nanohybrids: metal-free photocatalysts for solar-to-hydrogen peroxide energy conversion with 0.2% efficiency, J. Am. Chem. Soc. 138 (2016) 10019–10025.

[9] Y. Xiao, G. Tian, W. Li, Y. Xie, B. Jiang, C. Tian, D. Zhao, H. Fu, Molecule self-assembly synthesis of porous few-layer carbon nitride for highly efficient photoredox catalysis, J. Am. Chem. Soc. 141 (2019) 2508–2515.

[10] W.J. Ong, L.L. Tan, Y.H. Ng, S.T. Yong, S.P. Chai, Graphitic carbon nitride (g-C_3N_4)-based photocatalysts for artificial photosynthesis and environmental remediation: are we a step closer to achieving sustainability? Chem. Rev. 116 (2016) 7159–7329.

[11] J. Fu, J. Yu, C. Jiang, B. Cheng, g-C_3N_4-based heterostructured photocatalysts, Adv. Energy Mater. 8 (2018), 1701503.

[12] W. Zhen, L. Meili, Z. Zijian, Y. Wenqing, T. Hongwei, Z. Yongfa, Efficient visible-light-driven selective oxygen reduction to hydrogen peroxide by oxygen-enriched graphitic carbon nitride polymers, Energy Environ. Sci. 11 (2018) 2581–2589.

[13] S. Wu, H. Yu, S. Chen, X. Quan, Enhanced photocatalytic H_2O_2 production over carbon nitride by doping and defect engineering, ACS Catal. 10 (2020) 14380–14389.

[14] L.F. de, L. e Freitas, B. Puértolas, J. Zhang, B. Wang, A.S. Hoffman, S.R. Bare, J. Pérez-Ramírez, J.W. Medlin, E. Nikolla, Tunable catalytic performance of palladium nanoparticles for H_2O_2 direct synthesis via surface-bound ligands, ACS Catal. 10 (2020) 5202–5207.

[15] J. Cai, J. Huang, S. Wang, J. Iocozzia, Z. Sun, J. Sun, Y. Yang, Y. Lai, Z. Lin, Crafting mussel-inspired metal nanoparticle-decorated ultrathin graphitic carbon nitride for the degradation of chemical pollutants and production of chemical resources, Adv. Mater. 31 (2019), 1806314.

[16] H. Zhu, Q. Xue, G. Zhu, Y. Liu, X. Dou, X. Yuan, Decorating Pt@cyclodextrin nanoclusters on C_3N_4/MXene for boosting the photocatalytic H_2O_2 production, J. Mater. Chem. A 9 (2021) 6872–6880.

[17] S. Asadzadeh-Khaneghah, A. Habibi-Yangjeh, S. Vadivel, Fabrication of novel g-C_3N_4 nanosheet/carbon dots/$Ag_6Si_2O_7$ nanocomposites with high stability and enhanced visible-light photocatalytic activity, J. Taiwan Inst. Chem. E 103 (2019) 94–109.

[18] Z. Li, B. Li, J. Chen, Q. Pang, P. Shen, Spinel $NiCo_2O_4$ 3-D nanoflowers supported on graphene nanosheets as efficient electrocatalyst for oxygen evolution reaction, Int. J. Hydrog. Energy 44 (2019) 16120–16131.

[19] Y. Liu, Y. Huang, X. Duan, Van der Waals integration before and beyond two-dimensional materials, Nature 567 (2019) 323–333.

[20] J. Low, J. Yu, M. Jaroniec, S. Wageh, A.A. Al-Ghamdi, Heterojunction photocatalysts, Adv. Mater. 29 (2017), 1601694.

[21] D. Huang, Z. Li, G. Zeng, C. Zhou, W. Xue, X. Gong, X. Yan, S. Chen, W. Wang, M. Cheng, Megamerger in photocatalytic field: 2D g-C_3N_4 nanosheets serve as support of 0D nanomaterials for improving photocatalytic performance, Appl. Catal. B: Environ. 240 (2019) 153–173.

[22] J. Xiong, X. Li, J. Huang, X. Gao, Z. Chen, J. Liu, H. Li, B. Kang, W. Yao, Y. Zhu, CN/rGO@BPQDs high-low junctions with stretching spatial charge separation ability for photocatalytic degradation and H_2O_2 production, Appl. Catal. B: Environ. 266 (2020), 118602.

[23] J. Liu, Y. Liu, N. Liu, Y. Han, X. Zhang, H. Huang, Y. Lifshitz, S.-T. Lee, J. Zhong, Z. Kang, Metal-free efficient photocatalyst for stable visible water splitting via a two-electron pathway, Science 347 (2015) 970–974.

[24] J. Ran, W. Guo, H. Wang, B. Zhu, J. Yu, S.Z. Qiao, Metal-free 2D/2D phosphorene/g-C_3N_4 van der waals heterojunction for highly enhanced visible-light photocatalytic H_2 production, Adv. Mater. 30 (2018), e1800128.

[25] Y. Zheng, Z. Yu, H. Ou, A.M. Asiri, Y. Chen, X. Wang, Black phosphorus and polymeric carbon nitride heterostructure for photoinduced molecular oxygen activation, Adv. Funct. Mater. 28 (2018), 1705407.

[26] Y. Jin, D.H. Keum, S.J. An, J. Kim, H.S. Lee, Y.H. Lee, A. Van Der Waals, Homojunction: ideal p-n diode behavior in $MoSe_2$, Adv. Mater. 27 (2015) 5534–5540.

[27] Z. Liu, G. Wang, H.S. Chen, P. Yang, An amorphous/crystalline g-C_3N_4 homojunction for visible light photocatalysis reactions with superior activity, Chem. Commun. 54 (2018) 4720–4723.

[28] Y. Yu, W. Yan, X. Wang, P. Li, W. Gao, H. Zou, S. Wu, K. Ding, Surface engineering for extremely enhanced charge separation and photocatalytic hydrogen evolution on g-C_3N_4, Adv. Mater. 30 (2018), 1705060.

[29] D. Zhao, Y. Wang, C.-L. Dong, Y.-C. Huang, J. Chen, F. Xue, S. Shen, L. Guo, Boron-doped nitrogen-deficient carbon nitride-based Z-scheme heterostructures for photocatalytic overall water splitting, Nat. Energy 6 (2021) 388–397.

[30] G. Liu, G. Zhao, W. Zhou, Y. Liu, H. Pang, H. Zhang, D. Hao, X. Meng, P. Li, T. Kako, J. Ye, In situ bond modulation of graphitic carbon nitride to construct p-n homojunctions for enhanced photocatalytic hydrogen production, Adv. Funct. Mater. 26 (2016) 6822–6829.

[31] N. Huo, G. Konstantatos, Ultrasensitive all-2D MoS_2 phototransistors enabled by an out-of-plane MoS_2 PN homojunction, Nat. Commun. 8 (2017) 572.

[32] J. Zhou, Y. Yang, C.Y. Zhang, A low-temperature solid-phase method to synthesize highly fluorescent carbon nitride dots with tunable emission, Chem. Commun. 49 (2013) 8605–8607.

[33] H. Li, G. Huang, H. Xu, Z. Yang, X. Xu, J. Li, A. Qu, Y. Chen, Enhancing photodegradation activity of g-C_3N_4 via decorating with S-doped carbon nitride quantum dots by in situ polymerization, J. Solid State Chem. 292 (2020), 121705.

[34] Q. Wu, J. Cao, X. Wang, Y. Liu, Y. Zhao, H. Wang, Y. Liu, H. Huang, F. Liao, M. Shao, Z. Kang, A metal-free photocatalyst for highly efficient hydrogen peroxide photoproduction in real seawater, Nat. Commun. 12 (2021) 483.

[35] W. Wang, J.C. Yu, Z. Shen, D.K. Chan, T. Gu, g-C_3N_4 quantum dots: direct synthesis, upconversion properties and photocatalytic application, Chem. Commun. 50 (2014) 10148–10150.

[36] Z.L. Wu, Z.X. Liu, Y.H. Yuan, Carbon dots: materials, synthesis, properties and approaches to long-wavelength and multicolor emission, J. Mater. Chem. B 5 (2017) 3794–3809.

[37] Z. Jin, Q. Zhang, L. Hu, J. Chen, X. Cheng, Y.-J. Zeng, S. Ruan, T. Ohno, Constructing hydrogen bond based melam/WO_3 heterojunction with enhanced visible-light photocatalytic activity, Appl. Catal. B: Environ. 205 (2017) 569–575.

[38] E. Jung, H. Shin, B.H. Lee, V. Efremov, S. Lee, H.S. Lee, J. Kim, W. Hooch Antink, S. Park, K.S. Lee, S.P. Cho, J.S. Yoo, Y.E. Sung, T. Hyeon, Atomic-level tuning of Co-N-C catalyst for high-performance electrochemical H_2O_2 production, Nat. Mater. 19 (2020) 436–442.

[39] J. Liu, T. Zhang, Z. Wang, G. Dawson, W. Chen, Simple pyrolysis of urea into graphitic carbon nitride with recyclable adsorption and photocatalytic activity, J. Mater. Chem. 21 (2011) 14398–14401.

[40] W. Che, W. Cheng, T. Yao, F. Tang, W. Liu, H. Su, Y. Huang, Q. Liu, J. Liu, F. Hu, Z. Pan, Z. Sun, S. Wei, Fast photoelectron transfer in (Cring)-C_3N_4 plane heterostructural nanosheets for overall water splitting, J. Am. Chem. Soc. 139 (2017) 3021–3026.

[41] H. Huang, K. Xiao, N. Tian, F. Dong, T. Zhang, X. Du, Y. Zhang, Template-free precursor-surface-etching route to porous, thin g-C_3N_4 nanosheets for enhancing photocatalytic reduction and oxidation activity, J. Mater. Chem. A 5 (2017) 17452–17463.

[42] Z. Lu, G. Chen, S. Siahrostami, Z. Chen, K. Liu, J. Xie, L. Liao, T. Wu, D. Lin, Y. Liu, T.F. Jaramillo, J.K. Nørskov, Y. Cui, High-efficiency oxygen reduction to hydrogen peroxide catalysed by oxidized carbon materials, Nat. Catal. 1 (2018) 156–162.

[43] M.J. Bojdys, J.O. Muller, M. Antonietti, A. Thomas, Ionothermal synthesis of crystalline, condensed, graphitic carbon nitride, Chem. - A Eur. J. 14 (2008) 8177–8182.

[44] Y. Wang, M.K. Bayazit, S.J.A. Moniz, Q. Ruan, C.C. Lau, N. Martsinovich, J. Tang, Linker-controlled polymeric photocatalyst for highly efficient hydrogen evolution from water, Energy Environ. Sci. 10 (2017) 1643–1651.

[45] W. Wang, G. Li, T. An, D.K.L. Chan, J.C. Yu, P.K. Wong, Photocatalytic hydrogen evolution and bacterial inactivation utilizing sonochemical-synthesized g-C_3N_4/red phosphorus hybrid nanosheets as a wide-spectral-responsive photocatalyst: The role of type I band alignment, Appl. Catal. B: Environ. 238 (2018) 126–135.

[46] G. Wang, Q. Sun, Y. Liu, B. Huang, Y. Dai, X. Zhang, X. Qin, A bismuth-based metal-organic framework as an efficient visible-light-driven photocatalyst, Chem. Eur. J. 21 (2015) 2364–2367.

[47] T. Sun, G. Zhang, D. Xu, X. Lian, H. Li, W. Chen, C. Su, Defect chemistry in 2D materials for electrocatalysis, Mater. Today Energy 12 (2019) 215–238.

[48] Y. Xu, X. Niu, H. Zhang, L. Xu, S. Zhao, H. Chen, X. Chen, Switch-on fluorescence sensing of glutathione in food samples based on a graphitic carbon nitride quantum dot (g-CNQD)-Hg^{2+} chemosensor, J. Agric. Food Chem. 63 (2015) 1747–1755.

[49] H. Sheng, H. Ji, W. Ma, C. Chen, J. Zhao, Direct four-electron reduction of O_2 to H_2O on TiO_2 surfaces by pendant proton relay, Angew. Chem. Int. Ed. Engl. 52 (2013) 9686–9690.

[50] S. Zhao, X. Zhao, H. Zhang, J. Li, Y. Zhu, Covalent combination of polyoxometalate and graphitic carbon nitride for light-driven hydrogen peroxide production, Nano Energy 35 (2017) 405–414.

[51] G.-h Moon, W. Kim, A.D. Bokare, N.-e Sung, W. Choi, Solar production of H_2O_2on reduced graphene oxide–TiO_2hybrid photocatalysts consisting of earth-abundant elements only, Energy Environ. Sci. 7 (2014) 4023–4028.

[52] Y. Shiraishi, S. Kanazawa, Y. Kofuji, H. Sakamoto, S. Ichikawa, S. Tanaka, T. Hirai, Sunlight-driven hydrogen peroxide production from water and molecular oxygen by metal-free photocatalysts, Angew. Chem. Int. Ed. Engl. 53 (2014) 13454–13459.

[53] L. Yang, G. Dong, D.L. Jacobs, Y. Wang, L. Zang, C. Wang, Two-channel photocatalytic production of H_2O_2 over g-C_3N_4 nanosheets modified with perylene imides, J. Catal. 352 (2017) 274–281.

[54] C. Chu, Q. Zhu, Z. Pan, S. Gupta, D. Huang, Y. Du, S. Weon, Y. Wu, C. Muhich, E. Stavitski, K. Domen, J.-H. Kim, Spatially separating redox centers on 2D carbon nitride with cobalt single atom for photocatalytic H_2O_2 production, PNAS 117 (2020) 6376–6382.

[55] C. Chu, D. Huang, Q. Zhu, E. Stavitski, J.A. Spies, Z. Pan, J. Mao, H.L. Xin, C. A. Schmuttenmaer, S. Hu, J.-H. Kim, Electronic tuning of metal nanoparticles for highly efficient photocatalytic hydrogen peroxide production, ACS Catal. 9 (2018) 626–631.

[56] Y. Chen, X. Bai, A review on quantum dots modified g-c3n4-based photocatalysts with improved photocatalytic activity, Catalysts 10 (2020) 142.